scientific reports

Check for updates

OPEN

Self-folding of thick paper via continuous solution supply analyzed by FTIR spectroscopy

Yuki Odagiri[1], Yuki Fukatsu[1], Hiroki Kawagishi[1], Yuhei Yamada[2] & Hiroki Shigemune[3]✉

Origami techniques can impart mechanical properties to sheet materials, and stimulus responsive self-folding enables their transformation into three-dimensional structures. For practical origami devices such as load bearing structures, packaging components, and soft robotic bodies, folding of thick sheets is essential because thicker materials provide the strength durability needed for reliable deployment. However, conventional one pass inkjet printing cannot achieve 180° folding even in 127 µm thick paper. We therefore set 153 µm as a challenging target thickness that exceeds the folding limit of previous inkjet-based approaches. To overcome this constraint, we propose a self-folding method based on continuous solution supply from wetted filter paper. Diffusion simulations show that continuous supply produces a deeper through thickness concentration profile that governs subsequent transport. Experiments show that this initial state strongly affects the folding outcome, enabling 180° folding under continuous supply. FTIR-ATR analysis provided key mechanistic insight, revealing that large folding angles arise when the difference in hydrogen bonding between the surfaces becomes small, indicating through-thickness homogenization of the chemical state. These findings show that continuous solution supply enables controlled folding in thick substrates, providing a route to programmable three-dimensional architectures for deployable origami devices.

Origami, a traditional Japanese art, has been thoroughly explored from both mathematical and engineering perspectives. Mathematically, it has been demonstrated that arbitrary three-dimensional structures can be constructed using origami technology[1]. From an engineering standpoint, various functional structures have been proposed, including elastic, expansive, rigid, and shock-absorptive ones, all of which can be imparted to sheet materials simply by folding[2–4]. In addition, origami devices with electrical functions can be created by embedding circuits. Origami devices with novel structural functionality are expected to find a wide range of applications in space[5], medicine[6], and agriculture[7], and they are currently being investigated from both mechanical and electrical engineering perspectives.

In the context of industrialization, one of the major challenges is the mass production of origami structures. Extensive research has explored the use of stimulus-responsive materials to achieve automatic folding by activating the material itself. Depending on the type of stimulus, sheets can self-fold through thermal activation[8], surface-tension-driven deformation[9], or chemically induced reactions[10]. The mechanical properties of such self-folded structures have been investigated[8,11], and their practical applications[12]are currently under development. For practical devices, self-folding of thick sheets is crucial because thicker substrates provide greater mechanical strength and structural integrity, both of which are essential for deployable origami systems. Dickey et al. proposed a method for self-folding thick sheets by analyzing thermal gradients in thermoresponsive materials[13].

Cellulose-based materials are gaining attention in the context of sustainable device development. The environmental compatibility of electronic devices has become a major concern with the rapid proliferation of edge devices driven by the Internet of Things (IoT). In the field of paper electronics, cellulose-based devices have been developed as biodegradable, combustible, and sustainable alternatives to conventional substrates[14–16]. We previously developed a method for creating self-folding paper devices via inkjet printing[17], enabling paper-based circuit boards to be transformed into three-dimensional origami devices. However, conventional inkjet printing has a limited solution-deposition capacity and therefore cannot provide sufficient penetration for thick paper substrates.

In this study, we achieved self-folding of 153-µm-thick paper by controlling the amount of applied solution. To enable sufficient penetration, we developed a continuous solution-supply method using solution-saturated

[1]Electrical Engineering and Computer Science, Graduate School of Engineering and Science, Shibaura Institute of technology, Tokyo 135-8548, Japan. [2]Research Center for Autonomous Systems Materialogy, Institute of Integrated Research, Institute of Science Tokyo, Yokohama 226-8501, Japan. [3]College of Engineering, Shibaura Institute of Technology, 3-7-5, Toyosu, Koto-ku, Tokyo 135-8548, Japan. ✉email: hshige@shibaura-it.ac.jp

filter paper. One-dimensional diffusion simulations confirmed that the presence of continuous supply establishes the initial through-thickness concentration distribution, consistent with the experimental observations. The printed region was analyzed using Fourier-transform infrared spectroscopy with an ATR accessory (FTIR-ATR), which revealed that the absorbance difference between the front and back surfaces decreases as the applied amount increases. A larger folding angle was obtained under conditions where the front–back absorbance became nearly identical, indicating that homogeneous through-thickness transport of the solution governs the self-folding behavior of thick paper. Because this method ensures deep penetration while remaining compatible with fine printing line widths, it provides a practical route toward robust energy-absorbing origami structures, high-performance cushioning and packaging materials, and mechanically durable substrates for soft-robotic applications.

Materials and methods

Self-folding process

Figure 1 illustrates the self-folding process of paper using an inkjet printer. Figure 1(a) shows the solution being ejected onto the paper surface. As the solution penetrates the sheet, Fig. 1(b) shows the permeated region expanding, generating an initial mountain fold. As the amount of retained solution gradually decreases, contraction begins, and Fig. 1(c) shows a transient state in which expansion and contraction momentarily balance, flattening the sheet. With further reduction of the retained solution, contraction becomes dominant, and Fig. 1(d) shows the sheet bending into a concave shape. Finally, plastic deformation in this concave configuration fixes the folded geometry. Because this deformation is mechanically robust, the resulting structure exhibits excellent compressive energy absorption properties[5].

Theoretical model of through-thickness transport in self-folding.

Here, we introduce the theoretical model describing the transport process relevant to self-folding. The applied solution is transported through the paper according to the one-dimensional diffusion equation[18]. When a paper sheet of thickness h is placed in an infinite reservoir of solution and the initial concentration inside the sheet is zero, the solution concentration C at through-thickness position z and time t is given by Eq. (1)[19,20]:

$$\frac{C}{C_s} = 1 - \frac{4}{\pi} \cdot \sum_{n=0}^{\infty} \frac{(-1)^n}{2n+1} \cdot \exp\left[\frac{-D(2n+1)^2 \pi^2 t}{h^2}\right] \cdot \sin\left[\frac{(2n+1)\pi z}{h}\right] \quad (1)$$

Where D is the diffusion coefficient, and h is the paper thickness; z denotes the through-thickness coordinate measured from one surface ($z = 0$ at the front face and $z = h$ at the back face). C_s denotes the constant surface concentration imposed at both faces.

Equation (1) indicates $C(z) \to C_s$ at any z when $t \to \infty$. However, the homogenization process is interrupted when there is drainage effect, which results in the formation of a solution-penetrated area and a non-penetrated area. When the cross section of paper is divided into two areas, Timoshenko's beam deformation Eq. (2) could be applied to calculate the bending deformation[21].

$$\frac{1}{\rho} = \frac{6\epsilon E_1 E_2 h_1 h_2 (h_1 + h_2)}{E_1{}^2 h_1{}^4 + 2E_1 E_2 h_1 h_2 \left(2h_1{}^2 + 3h_1 h_2 + 2h_2{}^2\right) + E_2{}^2 h_2{}^4} \quad (2)$$

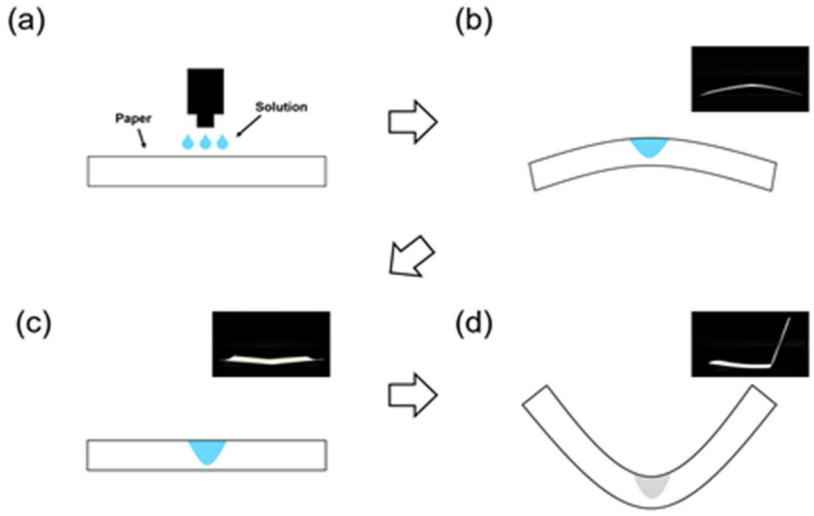

Fig. 1. Process of self-folding paper using inkjet printing. (**a**) Solution is ejected from the printer onto the paper surface. (**b**) The permeated region expands as the solution penetrates, generating an initial mountain fold. (**c**) Transient state in which expansion and contraction momentarily balance and the sheet becomes flattened. (**d**) Contraction becomes dominant as retained solution decreases, and plastic deformation in this concave configuration fixes the folded geometry.

where, ρ is the radius of deformation curvature of the paper, h_1 is the depth of the permeated solution, h_2 is the thickness of the non-permeated area, E_1 is the elastic modulus of the permeated area, E_2 is the elastic modulus of the non-permeated area, and ϵ is the strain induced with the reaction. Finally, the folding angle θ can be expressed using Eq. (3), which incorporates the printed line width l and the deformation curvature radius ρ.

$$\theta = \frac{l}{\rho} \tag{3}$$

As described above, the reactive and non-reactive areas are determined by liquid permeation, and the degree of folding is determined by the depth of the penetration. Conventionally, we have self-folded origami structures using the inkjet printer. The amount of applied solution was limited with the inkjet printing method, and a folding angle of $\theta = 180^\circ$ had not been demonstrated for the paper whose thickness was more than 150 µm. In this study, we have developed an experimental system for applying a large amount of the solution using the filter paper.

Printing procedures and measurement methods

Figure 2 presents the sample-preparation procedures and the measurement workflow used in this study. Figure 2(a) shows the printing process and workflow using an inkjet printer as the conventional approach. The target region on the paper is printed, and as the solution penetrates the sheet, the system transitions to the Free Reaction Phase. As penetration progresses and the amount of retained solution decreases, the paper undergoes self-folding, forming the origami structure. Because inkjet printing supplies only a limited amount of solution, the Loading Penetration Phase is absent. After structure formation is complete, the folding angle θ is measured using the image-analysis software ImageJ. Here, θ is defined as the angle between a straight line along the raised portion of the sheet and the horizontal.

To characterize the hydrogen-bonding states responsible for self-folding, the front and back surfaces of the printed region were analyzed using a Fourier-transform infrared (FTIR) spectrometer (IRAffinity-1 S, Shimadzu) equipped with an ATR accessory (Quest, Specac Ltd.). To evaluate the through-thickness penetration state, we compared the experimental results with the concentration distributions obtained from the diffusion simulations described later, and examined their relationship to the front–back chemical-state difference and the folding angle θ.

Figure 2(b) illustrates the printing process and workflow when using solution-saturated filter paper. In this method, placing the saturated filter paper on the sample introduces the Loading Penetration Phase. The solution supplied through the wet filter paper was deionized water. By controlling the filter-paper loading time

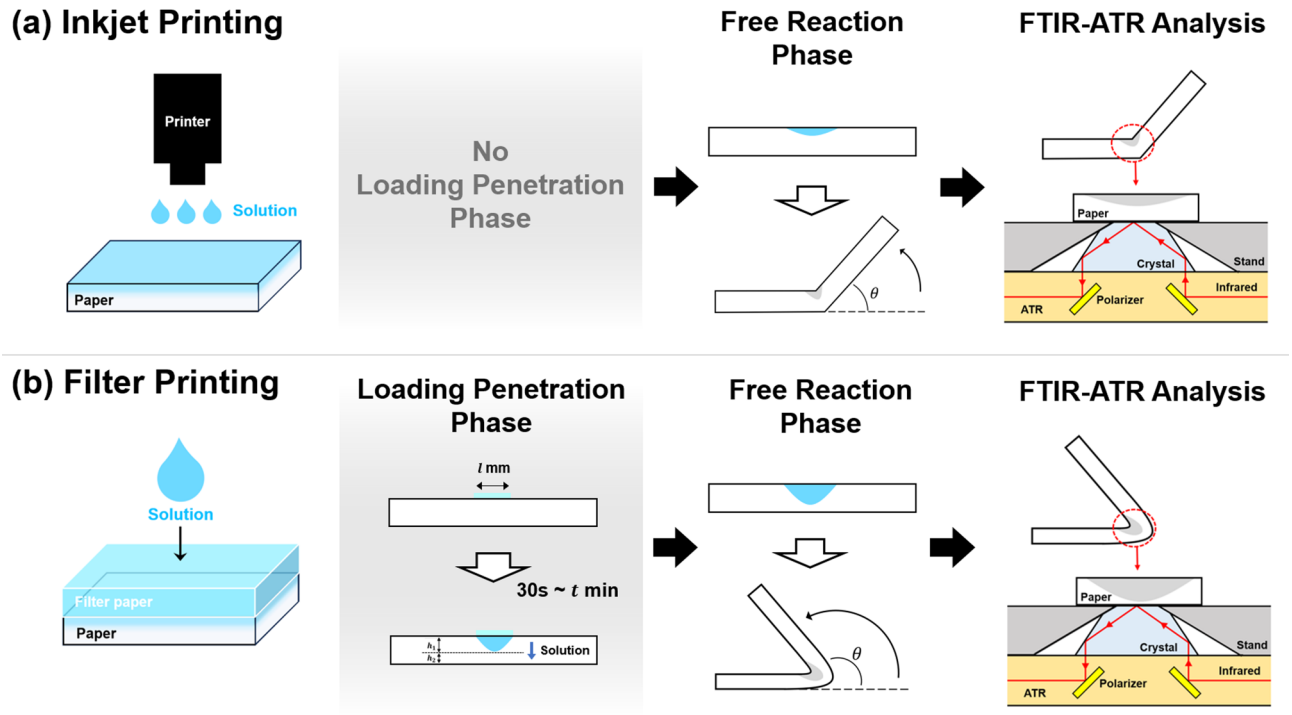

Fig. 2. (**a**) Printing process and measurement workflow in the inkjet method for self-folding of paper. (**b**) Printing process and measurement workflow in the filter-paper method. Use of the filter-paper method introduces the Loading Penetration Phase, and the solution is assumed to penetrate more deeply into thick paper. The mechanical deformation and associated changes in hydrogen-bond state were evaluated for each method.

(t = 0.5–20 min), continuous supply of solution into the paper is enabled; as a result, the solution is assumed to penetrate deeper than in the inkjet-printing scheme shown in Fig. 2(a). After removing the filter paper, the system transitions to the Free Reaction Phase, analogous to the inkjet method, and self-folding is completed. The subsequent measurement procedure is identical to that in Fig. 2(a), ensuring consistent quantification. For a fair comparison with the inkjet method, we used paper substrates that remain compatible with stable inkjet patterning, and the substrate thickness was selected within this common material condition.

Results and discussion

Diffusion simulations for inkjet and filter-paper methods

In this section, to quantitatively compare the penetration behaviors of thick paper in the inkjet and filter-paper methods, one-dimensional diffusion simulations were performed and the time evolution of the through-thickness concentration C was evaluated. Here, C is defined as the concentration contributing to diffusion. The z-axis was taken along the paper thickness $h = 153\ \mu\mathrm{m}$. The saturation concentration at surface is set to $C = 1$, and computations were carried out using the finite difference method. The governing equation used was as follows. Equation (1) gives an analytical solution for ideal diffusion, whereas Eq. (4) introduces loss term for simulation.

$$\frac{\partial C}{\partial t} = D\nabla^2 C - k_{loss}C \tag{4}$$

In the paper used in this study, in-plane spreading of the supplied solution was negligible. Experimentally, no noticeable in-plane penetration beyond the intended folding region was observed, either during the wet filter-paper supply or during inkjet printing. Therefore, the transport process could be reasonably treated as one-dimensional diffusion in the thickness direction.

Within the paper, not only diffusion occurs, but also trapping within the fibers and evaporation, causing the amount of moisture contributing to diffusion to decrease. k_{loss} is an effective parameter that represents that the apparent decrease in free solution arising from the trapping and evaporation. In the inkjet method simulation, the initial condition at $t = 0\ \mathrm{s}$ was set to $C = 1$ at the surface $z = 0$ and $C = 0$ in the interior, representing penetration into the interior driven by diffusion from the surface concentration $C = 1$. A diffusion coefficient $D = 1.0\ \mu\mathrm{m}^2\ \mathrm{s}^{-1}$ was used. Because the purpose of this section is a relative comparison of penetration behaviors under different supply conditions, rather than an experimental identification of D, this value was treated as a fixed parameter and used in both simulations to define a common time scale. As an order-of-magnitude reference, moisture diffusion coefficients reported for bulk cellulose films are $D = 0.5 \sim 1.5\ \mu\mathrm{m}^2\ \mathrm{s}^{-1}$, which is comparable to $D = 1.0\ \mu\mathrm{m}^2\ \mathrm{s}^{-1}$ used here[22]. In the filter-paper method simulation, as the Loading Penetration Phase, a continuous supply $C = 1$ was applied at the surface $z = 0$ for $-300\ \mathrm{s} \leq t \leq 0\ \mathrm{s}$, and k_{loss} was set to 0 assuming suppression of surface evaporation by the filter paper. Subsequently, a transition to the Free Reaction Phase occurred, the initial condition was set to $C(z,\ 0)$ at the end of the Loading Penetration Phase, and the evolution of the concentration profile was evaluated by diffusion with disappearance governed by $k_{loss} = 1.0 \times 10^{-3}\ \mathrm{s}^{-1}$.

Time–depth diffusion behavior in one-dimensional simulations.

Figure 3 shows the simulation results for the through-thickness concentration $C(z,\ t)$ obtained under the above simulation conditions. Figure 3(a) presents the results for the inkjet method. The penetration front remains near the surface, and the concentration gradient relaxes over time due to diffusion into the interior. Because the supply is transient, a wide high-concentration region across the thickness does not develop. Figure 3(b) shows the results for the filter-paper method. Owing to the Loading Penetration Phase, the penetration front advances deeper over time, and by $t = 0\ \mathrm{s}$ a wide high-concentration region across the thickness has already formed. After the transition to the Free Reaction Phase, the concentration field gradually becomes uniform; however, because the initial imbibed amount is large, the high-concentration region remains relatively wide. These results indicate that, in the filter-paper method, the penetration state at the start of the Free Reaction Phase differs markedly from that in the inkjet method, demonstrating the effect of continuous supply into the deeper region of the thick paper.

Figure 4 visualizes the diffusion behavior in the inkjet and the filter-paper method as a function of time. Figure 4(a) and 4(c) show the time evolution of the concentration at each depth, and Fig. 4(b) and 4(d) present concentration heat maps of penetration depth versus time. Figure 4(a) and 4(b) summarize the results for the inkjet method. In Fig. 4(a), the concentration is plotted at five positions from the top surface (z = 0 μm) to the deepest point ($z = 153\ \mu\mathrm{m}$): 0, 37.5, 74.9, 112.4, and 153 μm. Immediately after printing, the concentration at $z = 0\ \mu\mathrm{m}$ dropped rapidly. By contrast, in the mid-depth region ($z \geq 37.5\ \mu\mathrm{m}$) it remained below 0.1 throughout, indicating that in the inkjet method the front does not advance beyond approximately 37.5 μm in depth. Figure 4(b) presents the time–depth heat map for the inkjet method and shows that the penetration front remains nearly stationary, with minimal advance into the thickness direction. These results indicate that, in the inkjet method, the solution is essentially confined to the surface and does not sufficiently penetrate the sheet.

Figure 4(c) and 4(d) show the results for the filter-paper method. Figure 4(c) presents the time evolution of the concentration at five locations (0, 37.5, 74.9, 112.4, and 153 μm) during the Loading Penetration Phase ($-300\ \mathrm{s} \leq t < 0\ \mathrm{s}$) and the Free Reaction Phase ($0\ \mathrm{s} \leq t \leq 400\ \mathrm{s}$). From the mid-depth to the deep region ($37.5 - 153\ \mu\mathrm{m}$), the concentration gradually increases during loading and remains high after the transition to the Free Reaction Phase. Figure 4(d) is a time–depth heat map of the filter-paper method. It shows that the solution penetrates deeply during the Loading Penetration Phase and continues to advance in the Free Reaction Phase. At the start of the Free Reaction Phase (t = 0 s), a wide high-concentration region has already formed in the deep part of the sheet. This high-concentration region functions as a diffusion source. Thus, even though the

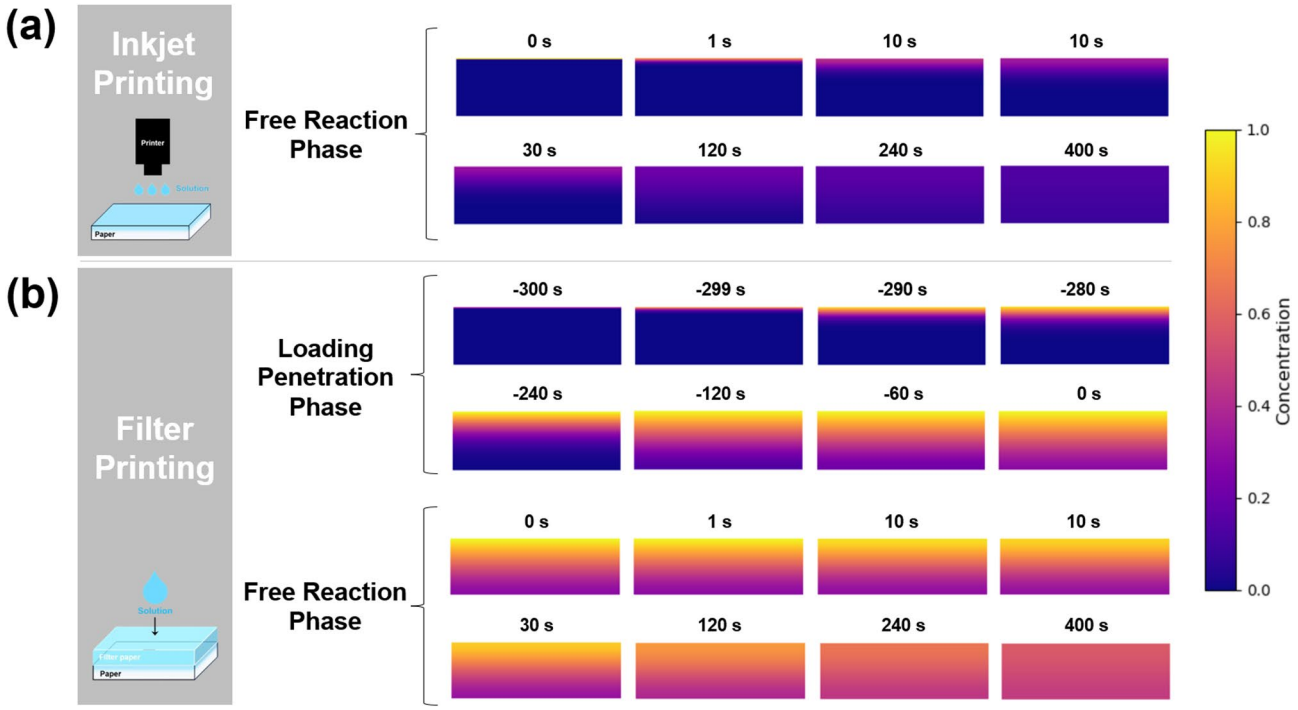

Fig. 3. Cross-sectional snapshots of the through-thickness concentration $C(z,\ t)$ from one-dimensional diffusion simulations. The colour map ranges from high concentration ($C = 1$) to low concentration ($C = 0$). (a) Inkjet method: immediately after printing, a transition to the Free Reaction Phase occurs ($0\ \mathrm{s} \leq\ t \leq\ 400\ \mathrm{s}$). The penetration remains confined near the surface; the concentration gradient relaxes over time due to diffusion into the interior, and a wide high-concentration region across the thickness does not develop. (b) Filter-paper method: Loading Penetration Phase ($-300\ \mathrm{s} \leq\ t < 0\ \mathrm{s}$) followed by Free Reaction Phase ($0\ \mathrm{s} \leq\ t \leq\ 400\ \mathrm{s}$). At $t = 0\ \mathrm{s}$, a wide high-concentration region across the thickness has already formed, and the highly imbibed state is maintained for an extended period.

overall concentration gradually decreases due to evaporation, the penetration front continues to progress, and a concentration gradient across the thickness is maintained.

These comparative results indicate that the presence or absence of continuous supply determines the initial through-thickness concentration distribution at the start of the Free Reaction Phase, which in turn governs the subsequent diffusion behavior. In the inkjet method, because the initial condition is confined to the surface layer, the penetration front quickly stalls. Therefore, to achieve reliable deformation behavior in thick paper, it is important to establish an initial state featuring deep penetration, which requires a continuous, rather than transient, supply condition. These findings provide a mechanistic basis for understanding the increase in folding angle and the reduction in front–back differences observed in the spectroscopic analysis described later. In summary, the filter-paper method establishes a deep, high-concentration region across the thickness during the Loading Penetration Phase, providing the diffusion-driven basis for larger folding angles in thick paper.

Control of printing density and folding angle

Figure 5 presents the self-folding behavior of 153 μm-thick paper obtained using the filter-paper method and its dependence on the printing density. Figure 5(a) shows a schematic of the filter-paper method and the time evolution of the printing density. Solution-saturated filter paper was placed on the top surface of the paper sample (60 mm × 90 mm, thickness 153 μm) to induce penetration. At the early stage of penetration, the paper tended to deform into a mountain fold toward the filter paper side, and even slight misalignment caused variability in the imbibed amount; therefore, both ends of the sample were weighted to suppress deformation. During the Loading Penetration Phase, the loading time t was varied to control the printing density P as defined by Eq. (5).

$$P = \frac{m}{la} \tag{5}$$

m [g] is the amount of absorbed solution, l [mm] is the horizontal width of the printing line, and $a = 60\ \mathrm{mm}$ is the vertical width of the printing line.

Figure 5(a) shows the time variation of the printing density P as a function of the filter-paper loading time t. The measurements showed that, for the line widths examined in this study, the printing density P increased consistently with the loading time t and exhibited no systematic dependence on the line width l. This trend indicates that suppressing out-of-plane bending with weights stabilized the penetration process. As a result, a clear correlation between the loading time t and the printing density P was obtained. The maximum printing density of $P = 6.84 \times\ 10^{-5}\ \mathrm{g\ mm^{-2}}$ was achieved when $l = 5\ \mathrm{mm}$ with a loading time of 20 min.

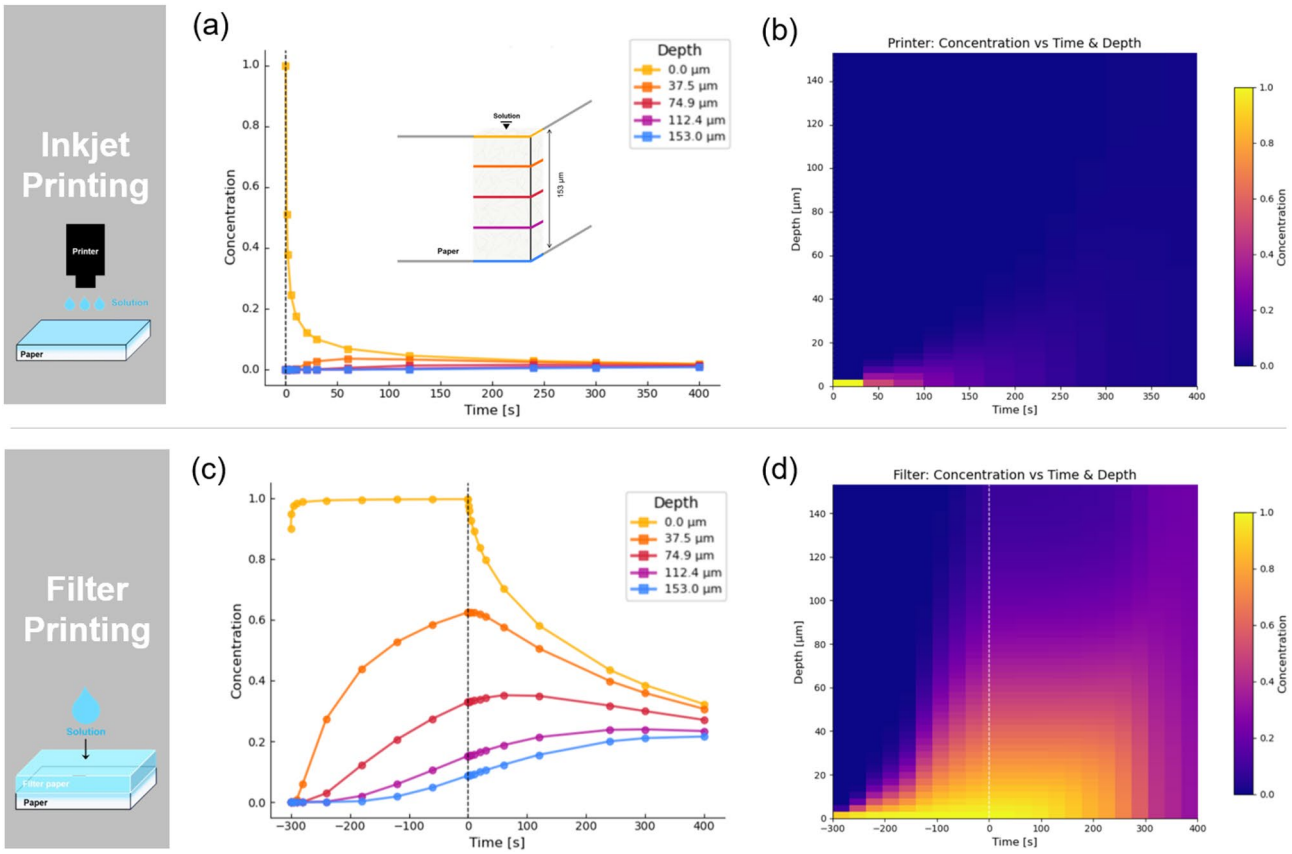

Fig. 4. Time evolution of the through-thickness concentration and time–depth heat maps for the inkjet method and the filter-paper method. (**a**) Time evolution of the concentration at each depth for the inkjet method. Immediately after printing, the surface-layer concentration drops sharply, while the mid-depth region remains low throughout. (**b**) Time–depth heat map for the inkjet method. Penetration in the thickness direction is minimal, and the penetration front remains stalled. (**c**) Time evolution of the concentration at each depth for the filter-paper method. The concentration gradually increases from the mid-depth to the deep region and remains high after the transition to the Free Reaction Phase. (**d**) Time–depth heat map for the filter-paper method. Owing to the Loading Penetration Phase, a wide high-concentration region across the thickness is established at $t = 0\ s$, and the penetration front continues to advance despite evaporation-induced concentration decrease.

For comparison, a single print using an inkjet printer with $l = 10\ \mathrm{mm}$ resulted in a printing density of $P = 6.22 \times 10^{-6}\ \mathrm{g\ mm^{-2}}$. Thus, the filter-paper method provides a printing density approximately 11 times higher than that of inkjet printing, demonstrating that it is a highly effective approach for supplying the solution.

Figure 5(b) shows the relationship the printing density P and the folding angle θ. For a given P, the folding angle θ becomes larger as the line width l increases, consistent with Eq. (3). A complete fold of $\theta = 180^\circ$ was achieved at $l = 10\ \mathrm{mm}$ and $P = 3.15 \times 10^{-5}\ \mathrm{g\ mm^{-2}}$. The complete folding ($\theta = 180^\circ$) was reproducible across multiple samples ($n = 3$). This result indicates that dense printing using the filter-paper method enables complete folding of 153 μm thick paper, which was not attainable with the previous inkjet method. Moreover, as P increases, a large θ can be obtained even when l is small, indicating that P serves as an effective tuning parameter that compensates for the reduced folding capability typically associated with narrow printing lines. The clear and monotonic relationship between P and θ also suggests high controllability. Within the paper size and experimental conditions investigated in this study ($90 \times 60 \times 0.153\ \mathrm{mm^3}$), the folding angle responds continuously to changes in the printing density, allowing the targeted design of θ.

FTIR-ATR assessment of front–back hydrogen-bond differences

FTIR-ATR analysis was performed using a Fourier Transform Infrared Spectrometer (IRAffinity-1 S, Shimadzu) equipped with an ATR accessory (Quest, Specac Ltd.) to measure the absorbance on both the front and back sides of the printed region. In FTIR-ATR measurements, the sample is irradiated with infrared light and the resulting absorbance spectrum is obtained based on molecular vibrational and rotational modes. Infrared light in the wavenumber range of 4000–400 $\mathrm{cm^{-1}}$ interacts with functional groups in cellulose, and FTIR-ATR has been widely used to elucidate hydrogen-bond interactions in cellulose-based materials[23,24]. Increases in hydrogen bonding, which are assumed to contribute to the self-folding mechanism, can be detected through

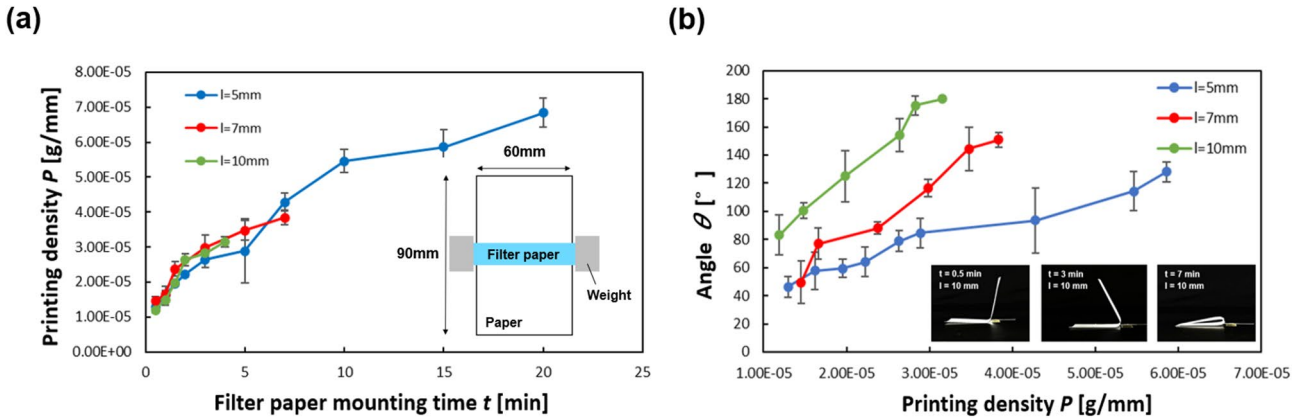

Fig. 5. Self-folding behavior of 153 μm-thick paper using the filter-paper method and its dependence on the printing density P. (a) Relationship between filter paper loading time t and printing density P. Under deformation suppression with weights, P increases monotonically with t, indicating that stable control of P is achievable using t as the control variable. (b) Relationship between printing density P and folding angle θ. Because P and θ show an approximately monotonic correlation within each series, θ can be designed by selecting an appropriate value of P.

changes in absorbance[25]. Therefore, analysing the functional-group-level interaction between cellulose and the absorbed solution enables evaluation of the relationship between the folding angle θ and the hydrogen-bond state within the paper. The measurement mode was absorbance, the apodization function was Happ-Genzel, the wavenumber range was $4000 - 400\ \mathrm{cm}^{-1}$, the resolution was $4\ \mathrm{cm}^{-1}$, and the number of integration was 16. All acquired spectra were subjected to smoothing and baseline correction before analysis.

In this study, the absorption band in the range $3700 - 2500\ \mathrm{cm}^{-1}$ was extracted, and the integrated spectral area within this range was defined as A_{total} and calculated using Eq. (6). Let the absorbance be $a\,(v)$, and let the wavenumber be $v\ \left[\mathrm{cm}^{-1}\right]$. Numerical integration of the discrete spectra was performed using the trapezoidal rule.

$$A_{total} = \int_{2500}^{3700} a\,(v)\,dv \tag{6}$$

The integrated area on the printed surface is denoted as A_{total}^{front}, and that on the back surface is denoted as A_{total}^{back}. The ratio R_{total} is defined as the quotient of these two values, as expressed in Eq. (7).

$$R_{total} = \frac{A_{total}^{front}}{A_{total}^{back}} \tag{7}$$

In the following discussion, R_{total} is used as the index for comparisons within the same method.

Figure 6(a) and (b) shows the IR spectra obtained from the paper self-folded using an inkjet printer (Brother, DCP-J540N). The printing density P was controlled by performing multiple overprints. A single print with $l = 10\ \mathrm{mm}$ and $P = 6.22 \times 10^{-6}\ \mathrm{g\,mm}^{-2}$ resulted in a folding angle of $\theta = 33.1^\circ$, while five overprints with $l = 10\ \mathrm{mm}$ and $P = 3.11 \times 10^{-5}\ \mathrm{g\,mm}^{-2}$ yielded $\theta = 128.7^\circ$. The effect of evaporation during overprinting is considered negligible because the printing density for five overprints was approximately five times that of a single print. From Fig. 6, peaks attributed to O–H stretching (3700–2500 cm^{-1}) and C–H stretching (3080–2550 cm^{-1}) were observed, which are characteristic features of cellulose Iβ[26].

On the front side, the absorbance in the wavenumber region $3900 - 2700\ \mathrm{cm}^{-1}$, which is sensitive to hydrogen bonding, was higher than that on the back side of the printed area. This front–back difference was more pronounced at $\theta = 128.7^\circ$ than at $\theta = 33.1^\circ$. In inkjet printing, the amount of applied solution is small and readily evaporates, and no appreciable difference between the front and back spectra was observed at $\theta = 33.1^\circ$. However, after five overprints, a clear absorbance difference appeared at $\theta = 128.7^\circ$. Quantification of this trend by integrating the spectrum over 3900–2700 cm^{-1} yielded $R_{total} = 0.967$ for a single print and $R_{total} = 1.364$ for five prints, indicating a clear dominance of the spectrum on the printed side. In other words, the front–back difference increased markedly with the number of overprints.

Figure 6(c)(d) shows the IR spectra obtained from two self-folded samples produced by the filter paper printing method. Figure 6(c) corresponds to a sample folded to $\theta = 83.2^\circ$ under the printing conditions $l = 10\ \mathrm{mm}$ and $P = 1.18 \times 10^{-5}\ \mathrm{g\,mm}^{-2}$. Figure 6(d) presents the spectrum for a sample folded to $\theta = 180^\circ$ under the conditions $l = 10\ \mathrm{mm}$ and $P = 3.15 \times 10^{-5}\ \mathrm{g\,mm}^{-2}$. The spectra are shown for the wavenumber range $4000 - 400\ \mathrm{cm}^{-1}$, which includes absorption bands associated with hydrogen bonding.

For the sample with $\theta = 83.2^\circ$, a front–back absorbance difference was observed in the $3900 - 2700\ \mathrm{cm}^{-1}$ region attributed to O–H stretching. In contrast, the sample folded to $\theta = 180^\circ$ exhibited almost no front–back difference. Quantification at the same printed location using R_{total} showed that a loading time of 30 s yielded $R_{total} = 1.226$, indicating dominance of the printed side, whereas a loading time of 240 s resulted in

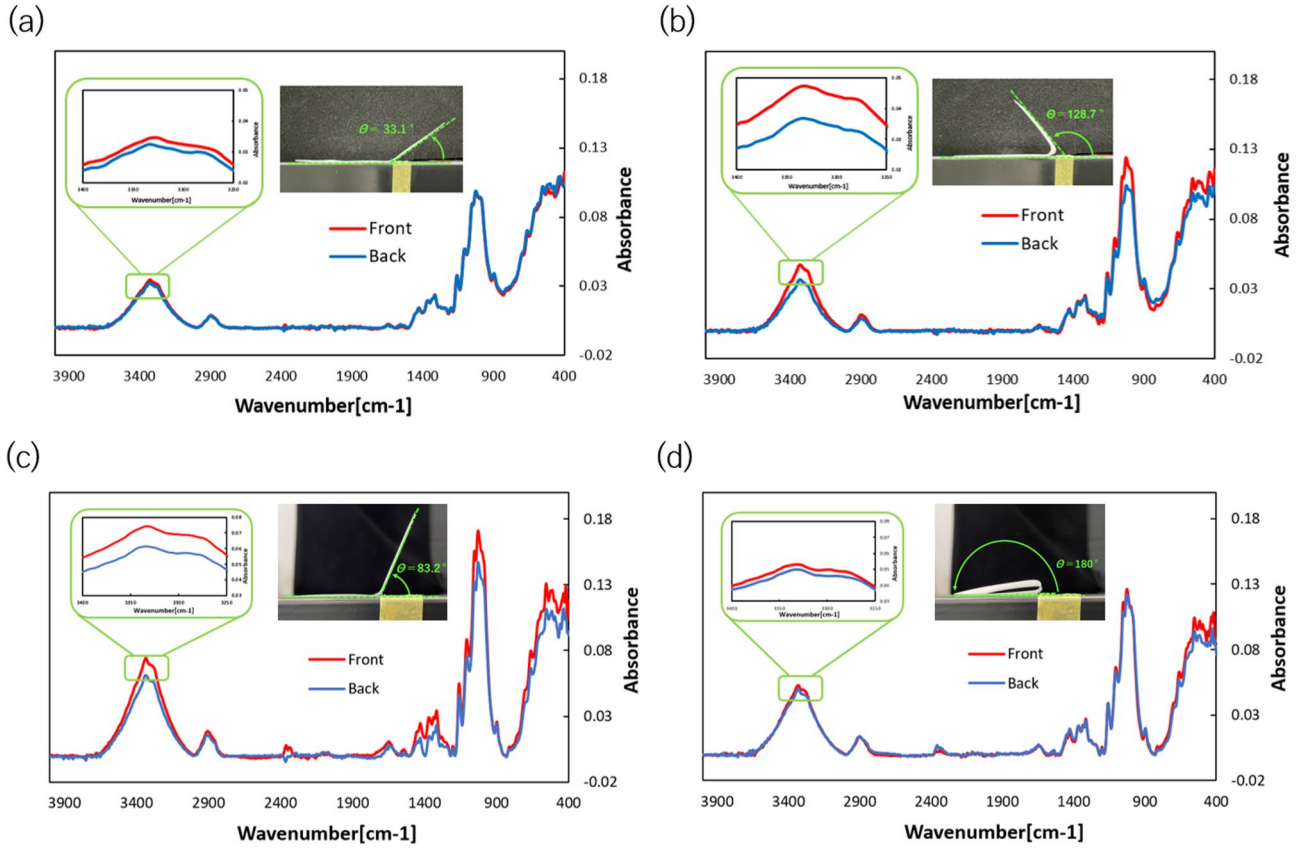

Fig. 6. IR spectra of the front and back sides of the printed area. (**a**) Inkjet method using a single print (θ = 33.1°). (**b**) Inkjet method using five overprints (θ = 128.7°). (**c**) Filter-paper method with a loading time of 30 s (θ = 83.2°). (**d**) Filter-paper method with a loading time of 240 s (θ = 180°). In the inkjet method, increasing the number of prints enhances the absorbance on the printed side. In the filter-paper method, the printed side is dominant at 30 s, while the front–back difference is almost eliminated at 240 s. All scale bars: 10 mm.

$R_{total} = 1.012$, where the front–back difference was nearly eliminated. These results indicate that extending the filter-paper loading time reduces the overall O–H absorption difference. As the printing density increased, the solution penetrated more deeply and reached the back side, resulting in a smaller front–back absorbance difference and a larger folding angle. Although the printing densities were almost the same, inkjet printing achieved $\theta = 128.7^\circ$ with $P = 3.11 \times 10^{-5}\,\mathrm{g\,mm^{-2}}$, whereas the filter-paper method produced complete folding ($\theta = 180^\circ$) at $P = 3.15 \times 10^{-5}\,\mathrm{g\,mm^{-2}}$. In the filter-paper method, the solution does not volatilize during application, and the penetration driving force at the interface remains higher, resulting in deeper permeation. In summary, FTIR-ATR measurements show that inkjet overprinting increases the front–back O–H absorbance contrast, whereas longer filter-paper loading times decrease this contrast and can nearly eliminate it, and these smaller front–back differences coincide with deeper penetration and larger folding angles in 153 μm-thick paper.

Demonstration of self-folding structures by filter-paper printing

Figure 7 presents a demonstration showing that the proposed filter-paper method enables fine self-folding of 153-μm-thick paper. Using this method, a Miura-ori structure and a corrugated structure were fabricated. The Miura-ori is a geometric pattern that allows easy unidirectional deployment and stowage while maintaining its shape through repeated folding and unfolding, and it is widely used in origami engineering and structural materials. In contrast, the corrugated structure forms periodic crests and troughs, provides high flexibility and stretchability, and is suitable for distributing bending stress and for surface functionalization.

Two printing patterns were designed in Adobe Illustrator, defining the Miura-ori as 80 mm × 120 mm and the corrugated structure as 148 mm × 120 mm (A5 size). Filter paper cut with a laser cutter was fixed on a water-repellent film, thoroughly wetted, and then placed on both sides of the sample to implement a 4 min Loading Penetration Phase. All demonstration structures were fabricated using the printing density of $P = 3.15 \times 10^{-5}\,\mathrm{g\,mm^{-2}}$. The continuous through-thickness supply of solution provided sufficient deep penetration to fold the thick paper even when narrow printing lines were used. Because folding proceeds with the printed side forming a valley, supplying the solution from both sides enables folding in both directions, making it possible to realize both the Miura-ori and corrugated structures. After removing the filter paper,

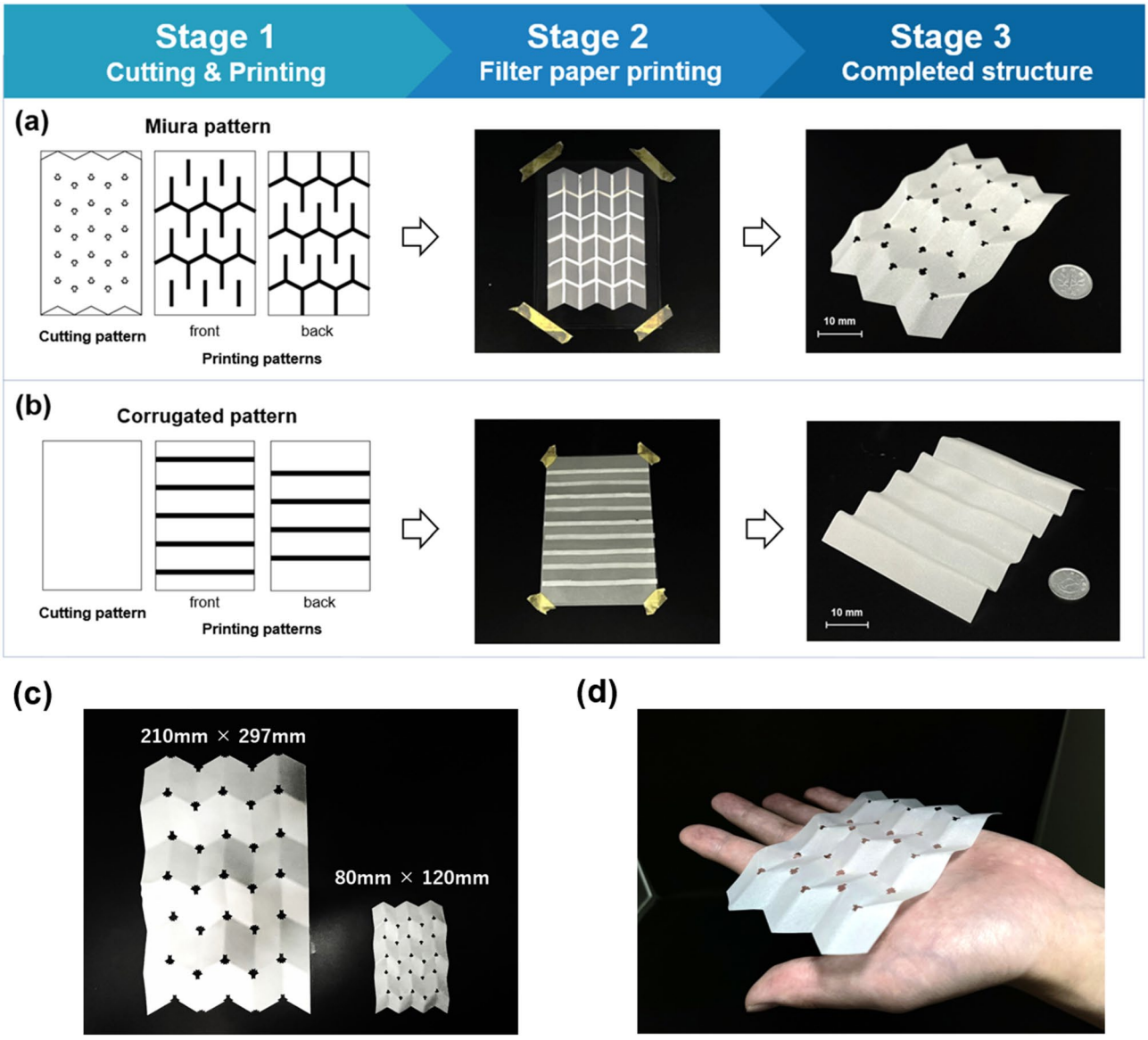

Fig. 7. Fabrication process and demonstration of fine self-folding structures using the filter-paper method. All samples were prepared by placing solution-saturated filter paper on both sides of the sheet and applying a 4 min Loading Penetration Phase. (**a**) Miura-ori: a fold pattern that enables repeated deployment and folding from a flat sheet; specimen size 80 mm × 120 mm. (**b**) Corrugated structure: a pattern with continuous periodic waves, giving the sheet flexibility and stretchability. (**c**) Size comparison of Miura-ori samples. A 210 × 297 mm specimen produced by the inkjet method (left) and an 80 × 120 mm specimen produced by the filter-paper method (right). The filter-paper method achieved self-folding even when the same crease pattern was scaled down. (d) An 80 × 120 mm specimen produced by the filter-paper method. Continuous crease formation and stable shape reproduction are visually confirmed even at this small size.

leaving the sample in the Free Reaction Phase at room temperature resulted in self-folding and completion of the structures.

Figure 7(a) shows a Miura-ori structure fabricated by the filter-paper method, and Fig. 7(b) shows a corrugated structure fabricated using the same approach. The vertex regions were intentionally removed in the Miura-ori design shown to suppress unstable folding and improve folding stability and reproducibility. In origami-based folding structures, vertex regions tend to experience stress concentration during deformation, which can lead to local damage or variability in the folding angle. The deep-penetration effect achieved with the filter-paper method generates a strong bending moment, demonstrating that fold structures can be formed even in 153 μm-thick paper. In Fig. 7(c), two Miura-ori specimens fabricated from 153 μm-thick paper are shown: a 210 × 297 mm specimen produced by the inkjet method and an 80 × 120 mm specimen produced by the filter-paper method. This comparison illustrates that self-folding can be achieved by the filter-paper method even when the pattern geometry is scaled down. Figure 7(d) presents an 80 × 120 mm specimen placed on a

hand, confirming continuous crease formation and stable shape retention even at reduced size. These results collectively indicate that the filter-paper method provides sufficient folding actuation through deep penetration driven by continuous supply, making it suitable for creating fine self-folding structures even when the geometric scale is reduced.

Conclusion

In this study, we proposed a self-folding method for 153-μm-thick paper based on continuous solution supply using filter paper and demonstrated complete 180° folding, which has not been achieved using conventional one-pass inkjet printing. Through one-dimensional diffusion simulations and FTIR-ATR analysis, we revealed that continuous supply forms a deeply penetrated through-thickness concentration profile, and that large folding angles appear under conditions where the front–back difference in hydrogen-bond density becomes negligible. Demonstrations further confirmed that, even when the printing line width is reduced, deep penetration provides sufficient bending capability to realize fine structures such as Miura-ori and corrugated patterns in 153-μm-thick paper. These findings show that continuous supply via filter paper is an efficient and scalable approach for self-folding of thick paper, expanding the potential of paper-based mechanical systems toward durable energy-absorbing structures, compact packaging materials, and soft-robotic components. The use of other solvents may affect not only diffusion behavior but elastic modulus changes, and reaction-induced deformation. The detailed coupled mechanisms governing how these effects interact to control the self-folding behavior remain to be clarified, and a systematic investigation using alternative or mixed solvents is left for future work. Future work will investigate the chemomechanical coupling of diffusion and deformation, broaden the range of foldable geometries, and further integrate modelling to quantitatively predict the folding response under various supply conditions, thereby deepening understanding of diffusion-induced self-folding in cellulose-based materials.

Data availability

The datasets used and/or analysed during the current study available from the corresponding author on reasonable request.

Received: 20 November 2025; Accepted: 13 February 2026
Published online: 15 February 2026

References

1. Demaine, E. D., Demaine, M. L. & Mitchell, J. S. B. Folding flat silhouettes and wrapping polyhedral packages: New results in computational origami. *Comput. Geom.* **16**, 3–21 (2000).
2. Filipov, E. T., Tachi, T. & Paulino, G. H. Origami tubes assembled into stiff, yet reconfigurable structures and metamaterials. *Proc. Natl. Acad. Sci. U. S. A.* **112**(40), 12321–12326 (2015).
3. Naritomi, D., Hosoya, N., Ando, G., Maeda, S. & Shigemune, H. Creation of origami-inspired honeycomb structure using self-folding paper. *Mater. Des.* **223**, 111146 (2022).
4. [4] Yasuda, H. et al. Origami-based impact mitigation via rarefaction solitary wave creation. *Sci. Adv.* **5** (5), eaau2835 (2019).
5. Chen, T., Bilal, O. R., Lang, R., Daraio, C. & Shea, K. Autonomous deployment of a solar panel using elastic origami and distributed shape-memory-polymer actuators. *Phys. Rev. Appl.* **11**(6), 064069 (2019).
6. Kuribayashi, K. et al. Self-deployable origami stent grafts as a biomedical application of Ni-rich TiNi shape memory alloy foil. *Mater. Sci. Eng. A, Struct. Mater. Prop. Microstruct. Process.* **419**(1–2), 131–137 (2006).
7. Geckeler, C. & Mintchev, S. Bistable helical origami gripper for sensor placement on branches. *Adv. Intell. Syst.* **4**(10), 2200087 (2022).
8. Liu, Y., Boyles, J. K., Genzer, J. & Dickey, M. D. Self-folding of polymer sheets using local light absorption. *Soft Matter*. **8** (6), 1764–1769 (2012).
9. Leong, T. G., Lester, P. A., Koh, T. L., Call, E. K. & Gracias, D. H. Surface tension-driven self-folding polyhedra. *Langmuir* **23** (17), 8747–8751 (2007).
10. Bao, N. et al. Gas-phase microactuation using kinetically controlled surface states of ultrathin catalytic sheets. *Proc. Natl. Acad. Sci. U. S. A.* **120**(19), e2221740120 (2023).
11. Fukatsu, Y. & Shigemune, H. Development of self-folded corrugated structures using automatic origami technique by inkjet printing. *Adv. Intell. Syst.* **4**(6), 2100260 (2022).
12. Felton, S., Tolley, M., Demaine, E., Rus, D. & Wood, R. A method for building self-folding machines. *Science* **345**(6197), 644–646 (2014).
13. Davis, D., Chen, B., Dickey, M. D. & Genzer, J. Self-folding of thick polymer sheets using gradients of heat. *J. Mech. Robot.* **8**(3), 031014 (2016).
14. Lien, D. H. et al. All-printed paper memory. *ACS Nano*. **8** (8), 7613–7619 (2014).
15. Koga, H. et al. Uniformly connected conductive networks on cellulose nanofiber paper for transparent paper electronics. *NPG Asia Mater.* **6** (3), e93–e93 (2014).
16. Tobjörk, D. & Österbacka, R. Paper electronics. *Adv. Mater.* **23** (17), 1935–1961 (2011).
17. Shigemune, H. et al. Printed paper robot driven by electrostatic actuator. *IEEE Robot. Autom. Lett.* **2**(2), 1001–1007 (2017).
18. Zou, Y., Maillet, B., Brochard, L. & Coussot, P. Fast transport diffusion of bound water in cellulose fiber network. *Cellulose* **30** (12), 7463–7478 (2023).
19. Hou, L., Feng, K., Wu, P. & Gao, H. Investigation of water diffusion process in Ethyl cellulose-based films by attenuated total reflectance fourier transform infrared spectroscopy and two-dimensional correlation analysis. *Cellulose* **21**, 4009–4017 (2014).
20. Fieldson, G. T. & Barbari, T. A. The use of FTi. r.-atr spectroscopy to characterize penetrant diffusion in polymers. *Polymer* **34** (6), 1146–1153 (1993).
21. Timoshenko, S. Analysis of bi-metal thermostats. *Josa* **11** (3), 233–255 (1925).
22. Guivier, M. et al. Water vapor transport properties of bio-based multilayer materials determined by original and complementary methods. *Sci. Rep.* **14**(1), 50 (2024).
23. Kondo, T. The assignment of IR absorption bands due to free hydroxyl groups in cellulose. *Cellulose* **4**, 281–292 (1997).
24. Watanabe, A. et al. Drying process of microcrystalline cellulose studied by attenuated total reflection IR spectroscopy with two-dimensional correlation spectroscopy and principal component analysis. *J. Mol. Struct.* **799**(1–3), 102–110 (2006).
25. Cichosz, S., Masek, A. & Dems-Rudnicka, K. Original study on mathematical models for analysis of cellulose water content from absorbance/wavenumber shifts in ATR FT-IR spectrum. *Sci. Rep.* **12**, 19739 (2022).

26. Maréchal, Y. & Chanzy, H. The hydrogen bond network in Iβ cellulose as observed by infrared spectrometry. *J. Mol. Struct.* **523** (1–3), 183–196 (2000).

Acknowledgements
This research was partially supported by JSPS KAKENHI Grant Numbers JP22K14226, New Energy and Industrial Technology Development Organization (NEDO) under Project JPNP20004, Fuji Seal Foundation, and International Research Center for Green Electronics Center.

Author contributions
Y.O., H.K., and H.S. conceived the research concept. Y.O., Y.F., H.K., and H.S. designed the methodology. Y.O., Y.F., and H.K. conducted the experiments, while Y.O., Y.Y. and H.S. performed the diffusion simulations. FTIR measurements and spectral analyses were carried out by Y.O., Y.F., and H.K. Figures and visualizations were prepared by Y.O. and H.S. The original draft of the manuscript was written by Y.O., Y.Y., and H.S., and all authors contributed to the review and editing of the manuscript. H.S. supervised the project. All authors discussed the results and approved the final version of the manuscript.

Declarations

Competing interests
The authors declare no competing interests.

Additional information
Correspondence and requests for materials should be addressed to H.S.

Reprints and permissions information is available at www.nature.com/reprints.

Publisher's note Springer Nature remains neutral with regard to jurisdictional claims in published maps and institutional affiliations.